AIAA Aviation
22-26 June 2015, Dallas, TX
33rd AIAA Applied Aerodynamics Conference

2015-3393

Optimization of Wind Turbine Airfoils Subject to Particle Erosion

Giovanni Fiore* and Michael S. Selig†
University of Illinois at Urbana-Champaign, Department of Aerospace Engineering, Urbana, IL 61801

An optimization of wind turbine airfoils subject to particle erosion is investigated. The erosive damage to the surface was represented by sand grains colliding with the blade leading edge. The optimization was performed by using a genetic algorithm approach (GA). A newly-written GA code was coupled with a two-dimensional inviscid flowfield solver (XFOIL) and with a particle dynamics code (BugFoil). The chosen scheme of the GA was based on random tournament selection. Each geometry was evaluated through a figure of merit that represented the airfoil fitness to damage and to aerodynamic performance when the airfoil is damaged. Multiple approaches to the optimization were taken. The initial step of this study involved optimization through geometry perturbations of the leading edge by means of Bezier curves. It was found that the leading edge shape modifications of existing airfoils increase the fitness of the airfoils subject to erosion. The second approach involved a crossover of existing airfoil geometries along with leading edge shape mutations, in order to expand the design space. The fitness of such airfoils was improved with respect to the first approach. However, for both these approaches the airfoil aerodynamic performance was disregarded, as they were intended to give insight on the optimal airfoil shapes. The final step of the study made use of an inverse airfoil design method (PROFOIL) to widen the design space even further. In this approach the aerodynamic performance of the airfoil was evaluated, and the GA became a two-objective optimization process (maximum lift-to-drag ratio, and erosive figure of merit). It was observed that bulbous upper leading edges, and slanted, flat lower leading edges allowed for best erosion performance. Moreover, it was seen that the airfoils with a positive camber required a smaller angle of attack to operate at the same lift coefficient, hence reducing the erosive damage experienced for sand grain impacts. The airfoils obtained from the inverse design GA algorithm were characterized by a lift-to-drag ratio greater than 310 for a Reynolds number of 5.84×10^6.

Nomenclature

AK	=	particle nondimensional mass
c	=	airfoil chord length
COE	=	Cost of Energy
C_d	=	airfoil drag coefficient
C_D	=	particle drag coefficient
C_l	=	airfoil lift coefficient
d	=	particle diameter
D	=	particle drag force
E	=	erosion rate
FOM	=	figure of merit
GA	=	genetic algorithm
$GAEP$	=	Gross Annual Energy Production
K	=	erosion rate constant

*Graduate Student (Ph.D.), Department of Aerospace Engineering, 104 S. Wright St., AIAA Student Member.
†Associate Professor, Department of Aerospace Engineering, 104 S. Wright St., AIAA Associate Fellow.
http://www.ae.illinois.edu/m-selig

LE = leading edge
m = particle mass
n = erosion rate velocity exponent
r/R = blade section radial location
Re = freestream Reynolds number
t = time
t/c = airfoil thickness-to-chord ratio
U = chordwise flowfield velocity component
V = chord-normal flowfield velocity component
V_∞ = freestream velocity
V_{imp} = particle impact velocity
V_s = particle slip velocity
x = chordwise coordinate
y = chordwise-normal coordinate
α = angle of attack
α_r = relative angle between flowfield and particle velocity
θ = impact angle
τ = nondimensional time
ω = weight used to compute FOM

Subscripts and superscripts

0 = initial state
l = lower limit
P = particle
tr = transition
u = upper limit

I. Introduction

Wind turbines used for eletrical power generation are subject to fouling and damage by airborne particles typical of the environment where the wind turbine operates. Throughout the 20-year lifespan of a wind turbine, particles such as rain, sand, hail, insects, and ice crystals are major contributors to a deterioration in turbine performance through local airfoil surface alterations.[1–6] Wind turbine blades accumulate dirt especially in the surroundings of the leading edge. In addition, temperature jumps and freeze-thaw cycles may cause smaller coating cracks to propagate, promoting coating removal and eventually delamination and corrosion damage due to exposure of the internal composite structure. The originally smooth surface of the blades may change considerably, and the increased roughness will cause a drop in gross annual energy production (GAEP) and an increase in cost of energy (COE).[7–13]

Modern trends in the wind turbine market have shown the benefits of offshore megawatt-scale wind turbine installations[14,15] in order to maximize GAEP while reducing COE. However, offshore locations are subject to more intense sand erosion than the majority of land installations.[13,16,17] Airborne sand particles collide with the blade and cause micro-cutting and plowing in the coating material[18,19] resulting in surface abrasion.[20,21] Such damage is particularly prominent at the outboard sections of the blade where the local relative velocity is larger compared with inboard sections.[16,22]

The weather conditions of a given wind farm site may vary substantially throughout the seasons. Throughout the world, another common damage scenario is represented by water-based particles, namely raindrops and hailstones.[23–25] When intense precipitation occurs, large raindrops may impact with the wind turbine blades and potentially promote internal panel delamination.[23,26] Even smaller raindrops increase the mechanical fatigue in the coating plastic materials[27,28] which translates into surface micro-cracking and a final erosive effect.[29]

The wind turbine industry has developed several devices to help mitigate the effect of airborne particles striking on the blade surface. In particular, chemical companies have commercialized leading edge tape products which allow for a convenient solution that is integrated into the blade maintenance cycle.[11,30,31] However, from the standpoint of

an aerodynamic designer such an approach may appear as a later fix. Hence, it is valuable to investigate which blade section geometry features allow for a minimization of the surface erosive damage.

The recent research has shown that the blade damage scenario is complex and multi faceted.[22–25,32] From an aerodynamic standpoint it must be noted that there exists a correlation between the blade flowfield and the particle interaction with the blade surface. In particular, small and lightweight particles are more susceptible to the aerodynamic flowfield than bigger and heavier particles. Therefore, a blade shape optimization to minimize the damage of any type of particle may be difficult to implement. For example, insects represent a complex scenario which is challenging to undertake due to the large variety of species and knowledge gaps concerning their aerodynamic characteristics. Other heavy particles such as hailstones are characterized by a trajectory that is fairly independent of the blade flowfield.[23,25] Little may be done from a shape optimization standpoint to minimize the damage to the panel due to hailstone strikes. However, the two particles that are most sensitive to the blade flowfield are sand grains and rain drops.[22,25] Both particles are associated with an erosion rate, hence allowing for an estimate of surface material loss. From an optimization perspective, such a parameter represents a direct feedback of the airfoil fitness with respect to particle erosion.

Large values of erosion rate are responsible for an earlier visible damage on the blade over time when compared with smaller values. Given the air quality characteristics of a chosen wind farm, a blade section geometry that is responsible for higher erosion rates will output less energy than a more damage-resilient blade over time. Such considerations motivate the investigation of optimum section geometries, under the novel perspective of airborne particle erosion. The goal of this study is to investigate the blade section geometry optimization for the case of sand erosion because sand represents the type of particle that is mostly susceptible to the blade aerodynamic flowfield, and hence the blade section geometry.

This paper is divided into five sections: the numerical method used is explained in Section II, the blade operating point, particle aerodynamics and damage models are introduced in Section III, while the results obtained are discussed in Section IV. Finally, conclusions are proposed in Section V.

II. Methodology and Theoretical Development

A. Particle Equations of Motion

In order to predict the erosive effect of sand grains on the blade surface, a lagrangian formulation code was developed in-house and named BugFoil.[22,25] BugFoil integrates a pre-existing particle trajectory code[33] and a customized version of XFOIL.[34] The local flowfield velocity components are obtained by querying the built-in potential flow routine of XFOIL from which the particle trajectory and impact location on the airfoil are computed.

In steady flight, the forces acting on the particle are perfectly balanced and perturbations to such forces are assumed to be additive to the steady-state forces. For these reasons the equations of motion may be expressed by neglecting the steady-state forces and may be written as functions of increments only.[35] In the current study, both raindrops and hailstones were treated as aerodynamic bodies whose only associated force is the aerodynamic drag D.

By applying Newton's second law along the particle trajectory in both chordwise x and chord-normal y directions, the following equations are obtained[18,22,36–38]

$$m_P \frac{d^2 x_P}{dt^2} = \Sigma F_x \tag{1}$$

$$m_P \frac{d^2 y_P}{dt^2} = \Sigma F_y \tag{2}$$

By projecting the drag of the particle D in both chordwise x and chord-normal y directions using the relative angle between particle and flowfield velocity α_r, the equations may be rewritten as

$$m_P \frac{d^2 x_P}{dt^2} = \Delta D \cos \alpha_r \tag{3}$$

$$m_P \frac{d^2 y_P}{dt^2} = \Delta D \sin \alpha_r \tag{4}$$

Given the particle velocity components U_P and V_P and given the velocity flowfield components U and V at a certain point along the trajectory, the particle slip velocity V_s can be expressed as

$$V_s = \sqrt{(U - U_P)^2 + (V - V_P)^2} \tag{5}$$

while the trigonometric functions in Eqs. 3 and 4 may assume the form

$$\cos \alpha_r = \frac{U - U_P}{V_s} = \frac{V_{rx}}{V_s} \tag{6}$$

$$\sin \alpha_r = \frac{V - V_P}{V_s} = \frac{V_{ry}}{V_s} \tag{7}$$

By expressing the particle aerodynamic drag D as a function of dynamic pressure and by substituting for the trigonometric functions, the Eqs. 3 and 4 may be rewritten as

$$m_P \frac{d^2 x_P}{dt^2} = \frac{1}{2}\, \rho\, V_s^2\, A_P\, C_D\, \frac{V_{rx}}{V_s} \tag{8}$$

$$m_P \frac{d^2 y_P}{dt^2} = \frac{1}{2}\, \rho\, V_s^2\, A_P\, C_D\, \frac{V_{ry}}{V_s} \tag{9}$$

To scale this problem in a non-dimensional fashion, non-dimensional time, space, and mass parameters can be introduced here

$$\tau = \frac{t\, U}{c} \tag{10}$$

$$\bar{x}_P = \frac{x_P}{c} \tag{11}$$

$$\bar{y}_P = \frac{y_P}{c} \tag{12}$$

$$AK = \frac{2\, m_P}{\rho\, A_P\, c} \tag{13}$$

Nondimensionalization of Eqs. 8 and 9 by a reference velocity U yield

$$\frac{d^2 \bar{x}_P}{d\tau^2} = \frac{1}{AK}\, \overline{V}_r\, C_D\, \overline{V}_{rx} \tag{14}$$

$$\frac{d^2 \bar{y}_P}{d\tau^2} = \frac{1}{AK}\, \overline{V}_r\, C_D\, \overline{V}_{ry} \tag{15}$$

which together represent a set of second-order, nonlinear differential equations. Once the particle drag coefficient is evaluated, the trajectory can be computed by numerically solving both x and y equations.

B. Sand Erosion

Upon impact, sand grains promote a mechanism of surface abrasion. Sand erosion is responsible for an increase in blade surface roughness and a decrease in structural stiffness. The parameter erosion rate E, defined as the removed mass of the target material divided by the mass of the impacting particle, is a function of particle impact velocity V_{imp} and angle at impact θ, and it is measured in units of (g/g).[19] The velocity V_{imp} is related to E through a power-law; whereas, the correlation with impact angle strongly depends on the eroded material properties. Most current materials used for wind blade coating are polyurethane derivatives[30] and show a primarily plastic erosion behavior with maximum erosion rate at θ = 30 deg.[39] Following the approach previously implemented by the authors,[22] the erosion rate for plastic materials is given by the equation[20,40–43]

$$E = K\, V_{imp}^n \tag{16}$$

where K and n are constants of the eroded material. The correlation between E and θ is implicit in the parameters K and n fitted at various impact angles and impact velocities. Similar to previous studies, the simulations were performed

by using linear-fitted erosion constants of ultrahigh molecular weight polyethylene (UHMWPE)[22] because it has the best performance of the polyethylene-based coatings, and because normal impacts cause small erosion rates.[40]

Each simulation is performed by placing a vertical array of sand particles five chord lengths upstream of the airfoil. Once the the simulation is initiated, the trajectory of the particles is evaluated and impingement is estimated. Given the angle and velocity at impact, E assumes different values in the region around the leading edge (LE), with a minimum associated with near-normal impact.

III. Aerodynamics of Damaged Airfoils and Analysis of Section Geometries

The design point for wind turbine airfoils is associated with the maximum aerodynamic efficiency $(C_l/C_d)_{max}$. To illustrate the significance of blade shape optimization it is of particular interest to predict the performance of blade sections in a damaged configuration (i.e., when the aerodynamic efficiency is reduced). In this section the aerodynamic performance of a damaged DU 96-W-180 are discussed.

A. Parametric Study on the Location of Fixed Transition

The erosion rate E curves due to sand on a DU 96-W-180 airfoil ($\alpha = 6.0$ deg) are shown in Fig. 1. The earliest damage to appear on the surface corresponds to the location of maximum erosion rate, when the blade is exposed to a prolonged erosion (as discussed by the authors in previous works[22]). In fact, at such locations, one can assume the quantity of eroded material to be the largest. Therefore, two fixed transition locations are considered on the upper and lower surfaces: $x^u_{tr} = 3.13$ % and $x^l_{tr} = 8.39$ %, respectively. These chordwise locations are obtained with BugFoil for a blade section located at $r/R = 0.75$ and $\alpha = 6$ deg, since it represents a suitable design point near $(C_l/C_d)_{max}$.

For a more general scenario, the effects on E due to the blade angle of attack, particle diameter, and section spanwise location (through local blade velocity) are shown in Fig. 2. It can be seen that an increase in α [Fig. 2(a)] is translated into a shift of the maximum erosion rate toward the leading edge for the upper surface and toward the trailing edge for the lower surface. On the other hand, an increase in particle diameter [Fig. 2(b)] is responsible for an increase in maximum E on both airfoil sides. Also, a shift of the peaks occurs toward the trailing edge on the upper surface and toward the LE on the lower surface. Lastly, an increase in blade velocity [Fig. 2(c)] causes an increase in maximum E that is roughly proportional to V^3_∞. In all cases, however, it can be noticed that the highest values of E are on the blade upper surface.

The current parametric study shows that it is relevant to investigate the effects of the chordwise position of the aerodynamic transition imposed by the erosion on the airfoil aerodynamic performance. Therefore, the aerodynamic performance of the DU 96-W-180 airfoil was analyzed with XFOIL by parameterizing the chordwise position of upper (U) and lower (L) fixed transitions. The effect on C_l/C_d due to the chordwise transition location can be seen in Fig. 3. Two curves are proposed, each obtained by modeling one surface with chordwise variable transition while imposing a fixed transition point due to sand erosion on the opposite surface ($x^u_{tr} = 3.13\%$, and $x^l_{tr} = 8.39\%$). It can be seen that the location of aerodynamic transition has a detrimental effect on $(C_l/C_d)_{max}$ as soon as the transition point moves from its natural location toward the LE. The most significant effect on the aerodynamic efficiency is due to the transition on the

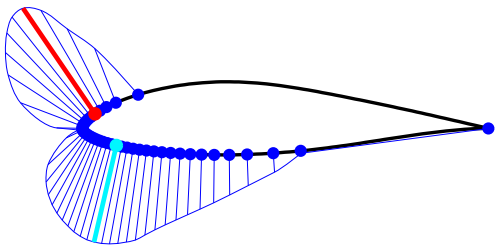

Figure 1. Erosion rate E curves on a DU 96-W-180 airfoil, $\alpha = 6.0$ deg. Red segment: upper maximum erosion rate (E^u_{max}); cyan segment: lower maximum erosion rate (E^l_{max}); blue circles: particle impingement points.

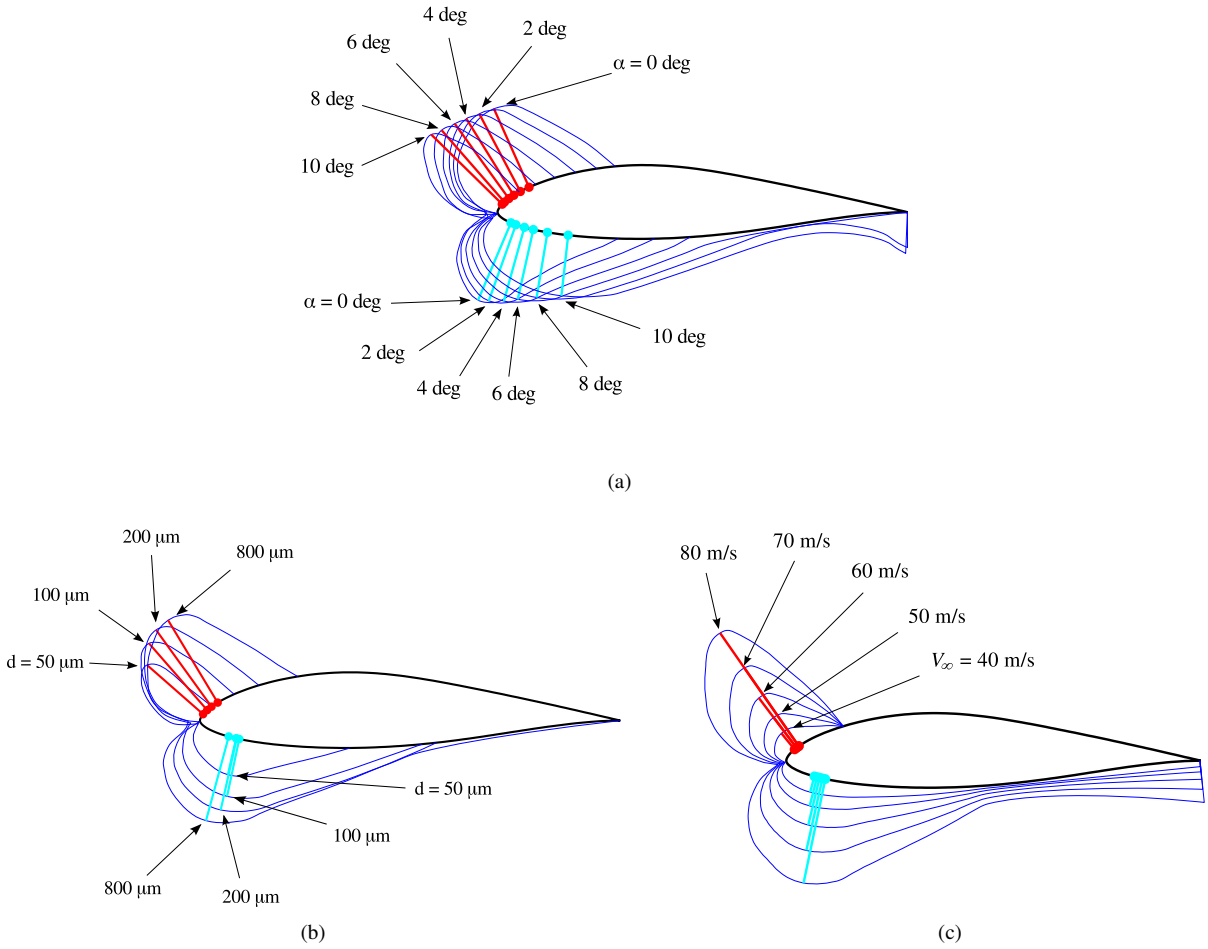

Figure 2. Effect of (a) blade angle of attack α, (b) sand grain diameter, and (c) blade velocity V_∞ on sand erosion rate E on the DU 96-W-180 airfoil.

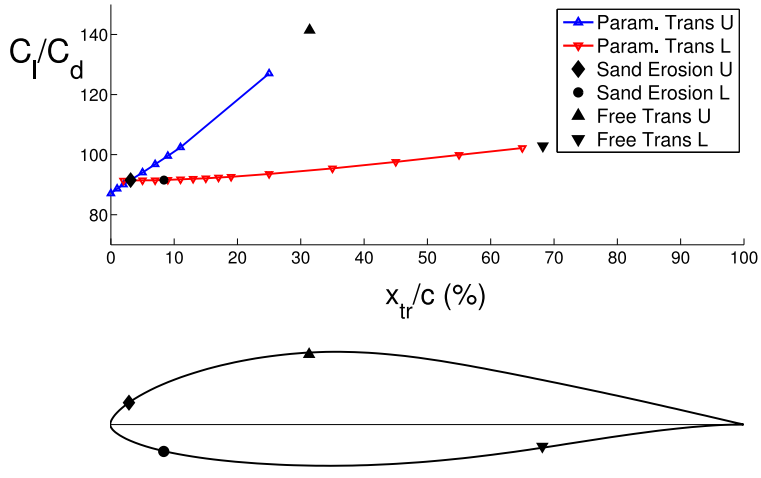

Figure 3. Effect on C_l/C_d of the chordwise location of fixed transition for the DU 96-W-180.

upper surface where a decrease of $C_l/C_d \approx 40\%$ is associated with an early upper transition. This figure is relevant in showing the magnitude of loss in GAEP of an eroded wind turbine. Similar values were obtained for the experimental investigation of damaged wind turbine airfoil performance carried out in previous studies by Sareen et al.[44]

B. Polars of a Blade Section Subject to Sand Erosion

The aerodynamic polars of the DU 96-W-180 airfoil (Fig. 1) are computed by using XFOIL for clean surface conditions, upper only fixed transition (U) (set by erosion), lower only fixed transition (L) (set by erosion), and both upper and lower fixed transitions (U+L). All computations were carried out at $Re = 6.88 \times 10^6$ as it represents a reasonable Reynolds number for a blade section located at $r/R = 0.75$ and $c = 1.7$ m.

Figure 4 shows the effects on the aerodynamic performance due to the various combinations of fixed transition. By assuming that the earliest damage in time would appear on the blade upper surface, an initial large increase in C_d is observed with respect to the clean configuration. Although smaller, a further increase in C_d is observed once the blade lower surface damage also appears. Finally, a drag coefficient approximately double the clean C_d for U+L transitions is observed. A larger contribution to C_d of the upper fixed transition may be explained by considering the pressure gradients acting on the upper surface and the longer curvilinear path covered by the boundary layer on the blade upper surface when compared with the lower surface. In fact, a thicker boundary layer would be observed on the upper surface when compared with the boundary layer on the lower surface. This would contribute to the overall form drag of the blade section which would increase more for the upper surface contribution than for the lower surface.

The aerodynamic efficiency C_l/C_d plot in Fig. 4 shows a similar effect to Fig. 3. It can be seen here that the drop in efficiency from clean to fixed upper transition (U) is drastic and brings the blade section to a $\approx$40 % penalization in C_l/C_d at $\alpha = 6$ deg. Once the lower blade transition is also fixed (U+L), a further decrease in aerodynamic efficiency is observed, bringing the blade section to approximately half the aerodynamic efficiency of the initial clean condition. Finally, by observing Fig. 5 an initial drop in C_l can be seen for upper transition, followed by a modest recovery when U+L-transitions are set. Such behavior may be due to the over-prediction in lift coefficient of XFOIL and should be verified with higher-order methods such as CFD. It should be noted now that the chronological history of damage on the blade section is not crucial to the present analysis. In fact, identical considerations may be drawn when considering an early lower damage and a later upper damage.

C. The Effect of Blade Shape on Sand Erosion

The scenario depicted in Sections III. A and III. B does not include the relationship of the blade section shape to sand erosion rate E. In the current section, the role of different geometry features with respect to sand erosion is investigated. An efficient way to compare the results is to fix the particle size, the freestream conditions, and the airfoil operating point while varying the airfoil geometry. At this point, it is significant to choose a design lift coefficient C_l rather than an angle of attack, since it gives a better indication of the blade operating conditions once the airfoil geometry is included in the blade design.

The analysis that has been carried out in previous studies[22,25] involved the Delft University wind turbine airfoil family applied to the damage problem.[12,45,46] Even though this choice of airfoils is currently representative of state-of-the-art wind turbines, it is somewhat limited when trying to investigate the geometric features that potentially minimize damage to blade sections. In fact, the NREL airfoil family offers a wider variety of upper and lower surface topology and curvature when compared with the DU family.[47–49] For such reasons, the NREL S family of airfoils is included here. Finally, because the most prominent effects of particle damage are seen when moving toward the blade tip, interest is aimed at optimizing outboard blade section geometries. A lift coefficient of 1.0 is chosen and the results are presented as a comparison between two pairs of airfoils as shown in Figs. 6, and 7. The erosion peaks on the airfoil upper side are denoted by red marks; whereas, the cyan lines denote peaks of the lower side. It should be noted that more airfoils were analyzed by the authors, but only four are shown in this section for brevity.

A DU 96-W-180 and a DU 96-W-212 are compared in Fig. 6 since they are characterized by very similar upper geometries, whereas the maximum thickness is due to the different curvature of the lower surface. The upper E peaks are virtually identical in value, shape, and chordwise maximum location. On the other hand, the more bulbous front part of the DU 96-W-212 promotes an erosion peak on the lower side that is noticeably farther downstream, when compared with the thinner DU 96-W-180 airfoil. In other words, the fuller shape of the airfoil lower side allows for the erosion peak to move downstream while also becoming flatter. No appreciable effect is detected as far as the maximum value of E on the blade lower side.

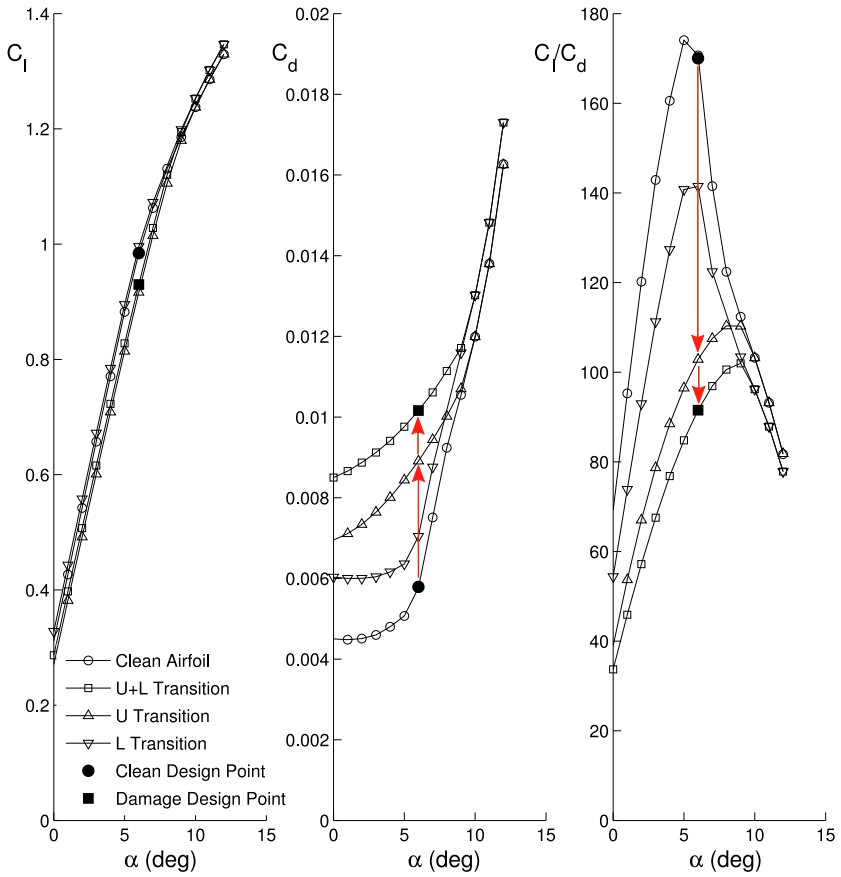

Figure 4. C_l, C_d, **and** C_l/C_d **curves of the DU 96-W-180 for clean and damaged conditions.**

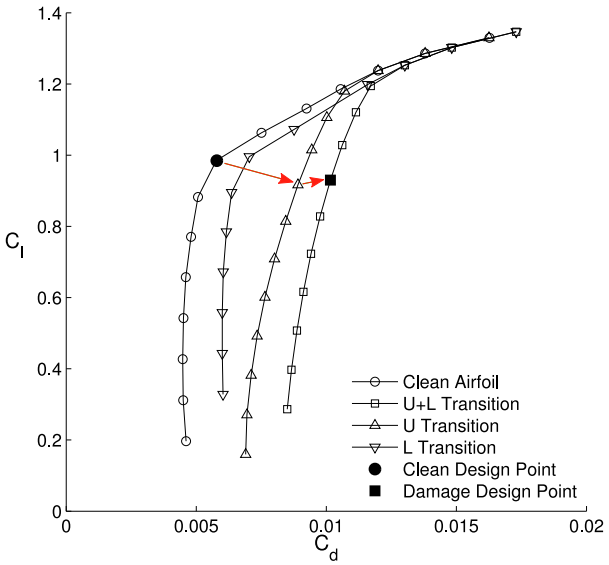

Figure 5. Drag polar of the DU 96-W-180 for clean and damaged conditions.

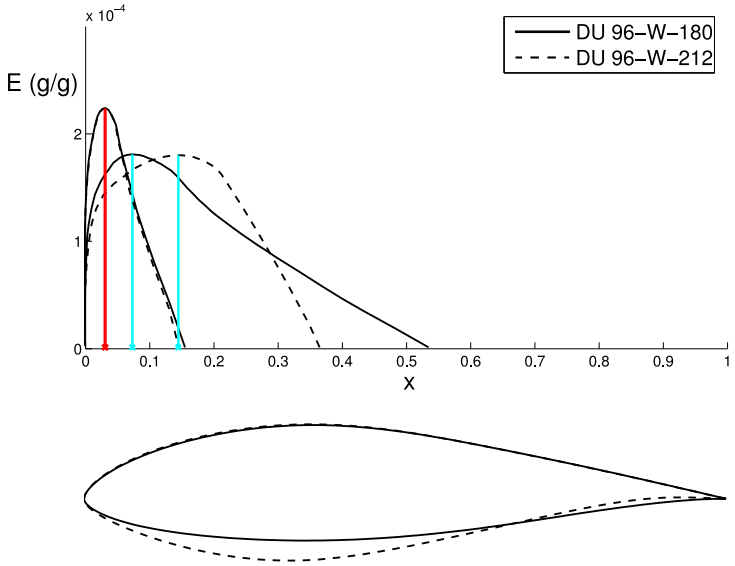

Figure 6. Erosion rate comparison for a DU 96-W-180 and a DU 96-W-212 at $C_l = 1.0$, effect of the lower side geometry. Upper side erosion rate peaks in red; lower side erosion rate peaks in cyan.

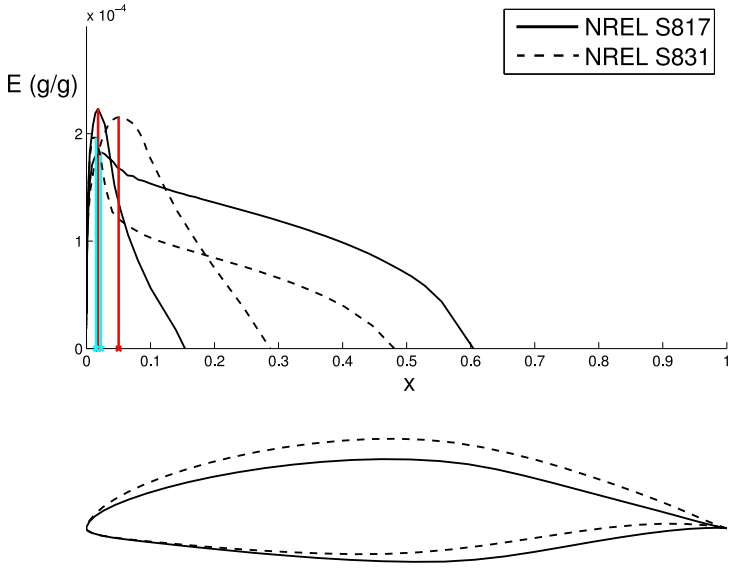

Figure 7. Erosion rate comparison for a NREL S817 and a NREL S831 at $C_l = 1.0$, effect of the upper side geometry. Upper side erosion rate peaks in red; lower side erosion rate peaks in cyan.

The situation is reversed when considering the airfoils NREL S817 and S831 in Fig. 7. Such airfoils have similar lower side geometries in the forward section, whereas the upper side is more bulbous for the NREL S831. The lower erosion peaks are virtually located at the same chordwise location, although the shape of E appears to be flatter for the NREL S817 airfoil. An important difference appears when considering the upper erosion peaks. Again, the bulkier geometry promotes an erosion peak farther downstream of the LE, when compared with the thinner section. Also, a slight drop in the maximum value of E is seen when considering the NREL S831.

D. Lessons Learned

The analysis of the previous sections highlights the role of the blade geometry with respect to erosion. It can be concluded that the chordwise location of maximum E is translated into appreciable effects on the aerodynamic behavior of the blade section once erosion is initiated. On the other hand, the maximum value of E is also driven by the blade section shape. In other words, the shape of the clean blade can dictate when and where the earliest damage would appear on the surface; the blade shape also dictates the performance in rough conditions due to the chordwise transition location on the upper and lower surfaces. Such an observation is an important feedback on blade geometry subject to sand erosion with respect to minimizing the loss of aerodynamic performance once the airfoil is damaged. In general, the blade designer would favor geometries that promote the lowest erosion peaks located as downstream as possible from the LE thereby allowing for better aerodynamic performance in rough conditions. From the comparison of the airfoils it can be concluded that:

- An important geometric feature that pushes the maximum-E location downstream is the LE slope. In particular, it appears that a more bulbous upper side allows for the maximum E to appear more downstream, when compared with thinner LE geometries.
- A similar observation could be made for the blade lower side. However, it was observed that the curvature of the blade may play an important role on both the shape of the erosion rate curve and the maximum location of E (see Fig. 6).
- The sensitivity of maximum E to variations in geometry is smaller when compared with the sensitivity of the chordwise location of maximum E. However, even small changes in maximum E translate into longer blade life, extending the clean, smooth conditions in which the turbine operate, yielding relatively higher values of GAEP over time.

E. Figure of Merit

The considerations of Section III. D pose a new problem that is quantifying the fitness of an airfoil subject to sand erosion. Generally, it would be significant to combine both the maximum value of E and the corresponding chordwise location to obtain a numerical insight on the airfoil erosion performance. In particular, a designer would want to penalize high values of erosion rate, while obtaining transition locations to be as downstream as possible on the blade surface. For these reasons, if such a designer would want to create the best erosion-resilient airfoil of those previously considered, he or she would need to combine the upper airfoil geometry of the NREL S831 [Fig. 7] with the lower geometry of the DU 96-W-212 [Fig. 6].

The proposed mathematical expression to obtain the fitness of an airfoil subject to sand erosion is the following figure of merit (FOM), that is

$$FOM = \frac{1}{E^u_{max}} \left(1.1 + x^u_{tr}\right)^{\omega_u} + \frac{1}{E^l_{max}} \left(1 + x^l_{tr}\right)^{\omega_l} \tag{17}$$

where ω_u and ω_l are the weights assigned to the upper and lower surface, respectively, in order to penalize large values of the chordwise location of transition x_{tr}. Such aspect is tied with the analysis of Section III. A and represents a powerful way to favor one side of the airfoil geometry with respect to the other. Because the upper side has shown a more important effect on the airfoil performance in damaged conditions compared with the lower side, the two chosen weights are $\omega_u = 5$ and $\omega_l = 1.5$.

To show the value of using FOM, a comparison of airfoils is proposed, with fixed $C_l = 1.0$. The airfoils discussed in Section III. C, along with NREL S804, S832, S813, and S810, are ranked based on the erosion performance

Table 1. Figure of Merit of Eight Airfoils Subject to Sand Erosion

Airfoil	t/c (%)	FOM	Rank
DU 96-W-180	18.0	14608	4
96-W-212	21.2	15237	1
NREL S817	16.0	13492	8
S831	18.0	14558	5
S804	17.9	14953	3
S832	15.0	13955	6
S813	16.1	13946	7
S810	18.0	15045	2

as summarized in Table 1. The best performing airfoil is the DU 96-W-212, characterized by $t/c = 21.2\%$ and representing the largest thickness amongst the tested airfoils. In light of the conclusions of Section III. D, the fact that the thickest airfoil would outperform all the competitors is not surprising. However, when selecting the blade section geometries to be used for the design of a wind turbine blade, the designer fixes the value of t/c for structural purposes, hence reducing the pool of airfoils to choose from.

A final consideration should be done on the aerodynamic performance of the airfoils. A proper selection of the most suitable geometries needs to be coupled with an analysis of C_l and aerodynamic efficiency C_l/C_d for a range of angles of attack. This procedure would avoid selecting damage-resilient geometries that however may penalize the ultimate goal of blade design being operated at high values of aerodynamic efficiency.

IV. Blade Section Shape Optimization

The objective of the blade section optimization is to maximize FOM. This is translated into a compromise between maximum erosion rate E_{max} and chordwise location of fixed transition x_{tr}. Modern optimization algorithms include gradient-based and genetic schemes. Gradient-based optimization schemes may be often challenging to implement as they require the exact mathematical model of the physics behind the problem. Because of the interplay between aerodynamics and particle dynamics, such approach is disregarded in favor of a genetic algorithm (GA) scheme.[50]

Based on the code developed for estimating wind turbine damage due to airborne particles (BugFoil),[22,25] a MATLAB wrapper has been implemented to perform GA optimization. Because the authors required complete freedom in the selection of the GA parameters, the wrapper has been written completely in-house, thus not using the available toolboxes of MATLAB.

Two main steps were involved in the optimization method implemented in this paper, with incremental degrees of complexity. The early phase is based on perturbations of existing airfoil geometries since it was expected to provide insight into the optimum airfoil geometries while being simple to implement. Such an approach can be regarded as a direct airfoil design GA optimization, aimed at maximizing FOM. In this initial approach the aerodynamic performance of the airfoils are not considered, as the scope is to obtain a first indication of the optimal geometries. The second part of the study deals with the more general and flexible theory of inverse airfoil design[51,52] coupled with genetic optimization.[53] In this phase, the aerodynamic performance of the airfoils are considered, hence resulting in a multi objective optimization. In particular, the objectives of the optimization are $(C_l/C_d)_{max}$ and FOM.

A. Genetic Optimization Through Geometry Perturbations

The first approach implemented for optimization makes use of random tournament selections to march through generations. The basic scheme of the genetic optimization through geometry perturbations follows these steps:

1. A pool of suitable airfoils is selected from the existing literature,
2. The geometric properties of two airfoils are combined in a random fashion to obtain a new generation (crossover),
3. Random perturbations on the airfoil properties may be inserted to increase species diversity (mutation),
4. The constraints are imposed: typically C_l or α, and $(t/c)_{max}$,

5. The particle code BugFoil is executed (evaluation),

6. *FOM* is computed and data is written into a logfile,

7. The best n specimens are selected for crossover for the next step (selection),

8. The algorithm proceeds back to step 2) until the number of maximum generations is reached or convergence is obtained.

Several questions arise on how to optimize a blade section shape. In particular, a designer may be interested in using existing geometries and modifying only a few aspects of those, for example the leading edge curves, the airfoil camber, or the airfoil thickness. Since the present study represents a novelty in wind turbine airfoil optimization, multiple approaches to the optimization process were investigated.

1. Optimization of the Leading Edge

The particle analysis carried out in previous studies highlighted the LE as the primary location of particle impact.[22,25] For such reasons, an initial investigation of solely the LE geometry for a given airfoil is performed. The idea here is to perform subsequent crossovers of an airfoil with a mutated version of itself, for a given number of generations.

However, a practical issue involving the LE optimization is finding suitable families of geometric curves to generate smooth, naturally-looking airfoils. In fact, even if the choice of algebraic n-degree polynomials may seem natural, it has several issues as far as continuity in the first and second derivative (C^1 and C^2), once the modified branch has to merge with the pre-existing part of the geometry. For these reasons, the Bezier polynomials were chosen to optimize the LE geometry. Such polynomials allow to fix the start and end points of a curve, while varying the curve path through the position of intermediate control points.[53–56] The number of Bezier control points dictates the degree of the Bezier polynomial. It should be noted that the higher the degree of the Bezier polynomial, the higher the number of convexities and concavities that a curve may have. Such considerations reduce the practical number of control points considerably. From a practical standpoint, once the LE curves of a given airfoil are obtained, a complete replacement of such a geometry may be performed while still maintaining continuity and shape regularity with the existing curves of the airfoil.

To obtain shape continuity and smoothness, two control points are fixed at the start and end points of the upper and lower LE geometries ($P1$ and $P5$ in Fig. 8), while two control points are placed strategically next to them, and named $P2$ and $P4$. $P2$ and $P4$ control the second derivative of the curve in the region where the modified LE has to merge with the existing geometry. To investigate the optimal LE shape with the GA scheme, the coordinates of the last control point $P3$ are randomly placed by the algorithm on a mesh of possible positions. The mesh is defined as a grid of coordinates within the most forward LE point, and the location of maximum thickness of the airfoil. By operating in such a way, the regularity of the LE curve is mantained to a reasonable extent even for extreme positions of the random control point $P3$. Moreover, it avoids the possibility of concave curves or very flat leading edges. Figure 9 shows the results in applying such an approach to the upper and lower curves of the DU 96-W-180 LE. As it can be

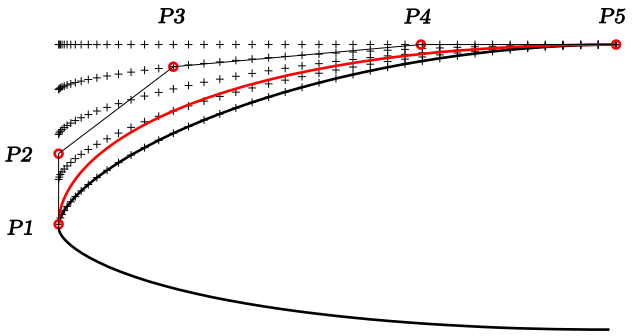

Figure 8. Modification of the LE geometry. Black solid line: original geometry; red line: modified geometry; red circles: Bezier control points; black crosses: possible positions of the random control point.

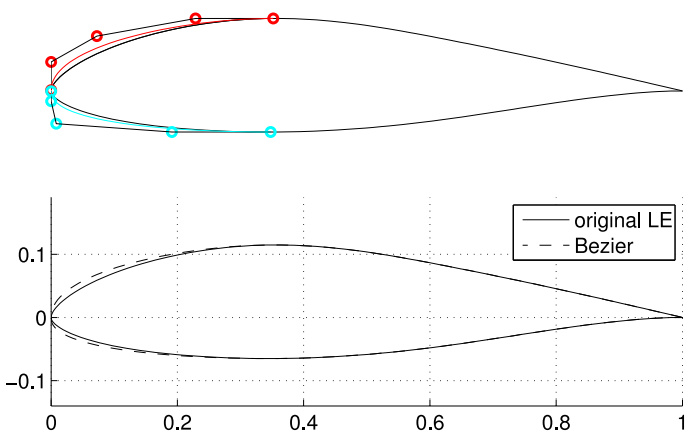

Figure 9. Bezier curves applied on the LE geometry of a DU 96-W-180 airfoil. Red circles: upper Bezier control points; cyan circles: lower Bezier control points.

seen in the lower part of the figure, a natural-looking airfoil is obtained for random positions of the upper and lower $P3$ points.

2. *Results*

Three airfoils are considered: the DU 96-W-180, the DU 96-W-212, and the DU 96-W-250 by moving from the blade outboard region toward the hub. The three airfoils differ in thickness (t/c). In fact, the outboard airfoil has a 18% thickness, followed by 21.2 %, and finally a 25% thick airfoil is used. Each optimization is run by iteratively performing a crossover of the airfoil with a mutated version of itself followed by the computation of FOM. The optimization is stopped once the maximum number of generations is reached, which in this case is 100.

The selected airfoils are optimized by mantaining the same inflow velocity and chord length, so that the results between airfoils are comparable, and the effects of the inflow velocity on the erosion rate E are the same. A 37-m wind turbine blade, with a tip-speed ratio of 8.7, and operating at 23 rpm is considered. The diameter of the sand grain used for the optimization is $d = 200$ μm, the inflow velocity is $V_\infty = 69.4$ m/s, the airfoil chord length is $c = 1.7$ m, and

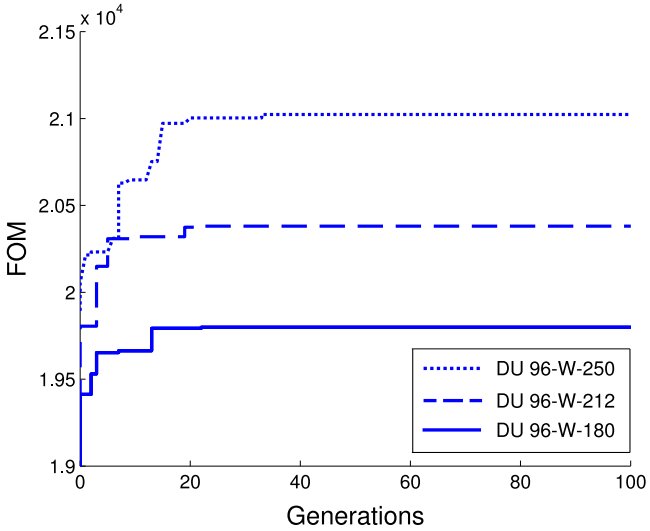

Figure 10. LE optimization: history of FOM for the three airfoils.

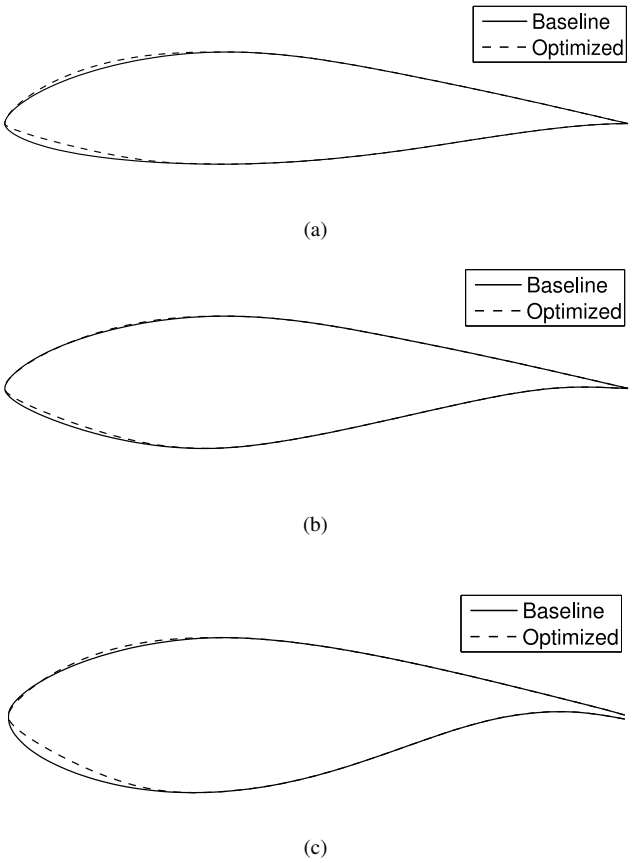

Figure 11. Optimized LE of (a) DU 96-W-180, (b) DU 96-W-212, and (c) DU 96-W-250; sand grain diameter $d = 200$ μm, $C_l = 1$.

the airfoils are tested at $C_l = 1$. By doing so, the airfoils operate with the same amount of circulation per unit span, hence the aerodynamic effects on the particle trajectories are comparable away from the surface. All simulations were performed with BugFoil[22,25] nested in a newly-written MATLAB GA routine. The evaluation of a single individual requires ≈ 6 sec computational time on a 8 Gb RAM Core i7 Linux machine running LinuxMint OS. On average, the runtime for each optimization was 3 hr.

Figure 10 shows the history of FOM with respect to the number of generations for the three airfoils. It can be observed that convergence is reached with ample margin on the maximum number of generations. The optimized leading edges are presented in Fig. 11 for the three airfoils. Despite the different thickness, the first common characteristic to all three airfoils is related to the curvature of the upper side of the LE. The optimized upper side appears more bulbous, especially for the DU 96-W-180 [Fig. 11(a)] and for the DU 96-W-180 [Fig. 11(c)] as compared with the original geometries. The second common characteristic is related to the flat, slanted lower side of the LE, visible in all three airfoils.

A comparison of FOM is reported in Table 2. The airfoil with the highest FOM is the DU 96-W-250, which is also the thickest airfoil of the three. Again, a thick airfoil allows the sand particles to slow down more, and offering near-normal particle impacts on the lower surface, thus mitigating the erosion effects when compared with thinner airfoils, as mentioned in Section III. E. Also, it can be seen that a consistent increase in FOM exists for the three airfoils when compared to their baseline.

The results for the LE optimization show that the observations of Section III. C are repeated. In particular, a high FOM can be obtained by allowing the sand particles to hit at a steep angle on the lower side, while offering moderate angles of impact on the upper side. Moreover, the lower side of the optimized airfoil, characterized by a flat, slanted surface may allow for a stronger decrease in particle velocity compared with more curved surfaces.

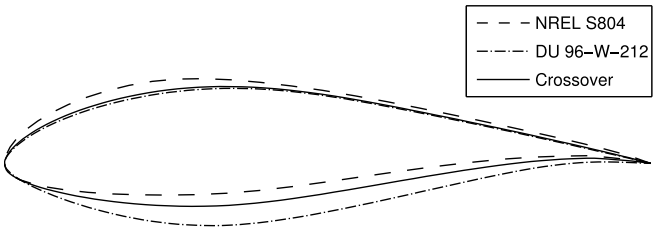

Figure 12. An example of the crossover operator: weighted average of a NREL S804 and DU 96-W-212 airfoils.

3. Global Airfoil Optimization

The optimization of the LE geometry only is restricting and prevents the analysis of larger design spaces. In this section, the optimization is performed by a crossover operator within a selected pool of airfoils with comparable thickness. The idea is to blend the airfoils by computing the random weighted average of the upper and lower geometries of the parent airfoils. Figure 12 shows the result of operating crossover on two fairly different geometries, the NREL S804 and the DU 96-W-212 geometry. The weighted average crossover allows for the child geometry to lie in between the geometry of the parents, while considerably expanding the design space of the geometries with respect to the LE optimization. Such approach makes it possible to only consider feasible geometries, enhancing the effectiveness of the optimization process by reducing the possibility of faulty airfoils.

A starting pool of six airfoils is selected with $t/c \approx 18\%$. The pool is composed by the following airfoils: DU 96-W-180, NREL S804, S810, S813, S817, and S831 (see Table 1). Two different optimization approaches are pursued. The simplest involves the crossover of unmutated parents only. Unmutated refers to geometries that are a linear combination of previous geometries (pure crossover). By doing so, an insight is expected regarding the fittest shapes for the upper and lower airfoil surfaces. The second approach involves also LE edge perturbations (crossover and mutation) in the form of Bezier curves, as explained in Section IV. A. 1. The second approach is expected to achieve better FOM values and give a clearer view of the optimal airfoil shape.

4. Results

Figure 13 shows the optimization history of FOM and geometry without LE perturbations [Figs. 13(a) and 13(b)], and with LE perturbations [Figs. 13(c) and 13(d)]. The convergence for the optimization with no LE perturbation [Fig. 13(a)] occurs at a faster rate than the convergence for the LE perturbations [Figs. 13(c)]. The presence of LE perturbations also allows for prominent jumps in the FOM curve.

Because the starting pool of airfoils is unchanged, a striking similarity between the two histories of geometry can be seen [Figs. 13(b) and 13(d)]. Due to its simplicity, the approach with no LE perturbations [Fig. 13(b)] shows fewer optimal shapes through the evolution when compared with the LE perturbation approach [Fig. 13(d)]. In fact, by focusing on the LE region, a more crowded scenario can be observed when the LE perturbations are used [Fig. 13(d)].

A comparison of the optimal geometries can be seen in Fig. 14. The LE appears more skewed on the upper side when the LE perturbations are used, as opposed to the fuller and more rounded LE of the other case. Such a shape, which can be thought of as a knee shape, allows for the peak of erosion rate E to move considerably downstream on the upper surface. Due to this fact, FOM can achieve considerably larger values when compared with the no LE perturbations approach as shown in Table 3. However, from an aerodynamic point of view, a knee shape is responsible

Table 2. Figure of Merit of the DU Family Airfoils Before and After Leading Edge Optimization

Airfoil	$FOM_{original}$	$FOM_{optimized}$	$\%\Delta_{FOM}$
DU 96-W-180	14,608	19,799	35.5
DU 96-W-212	15,237	20,380	33.7
DU 96-W-250	15,952	21,024	31.8

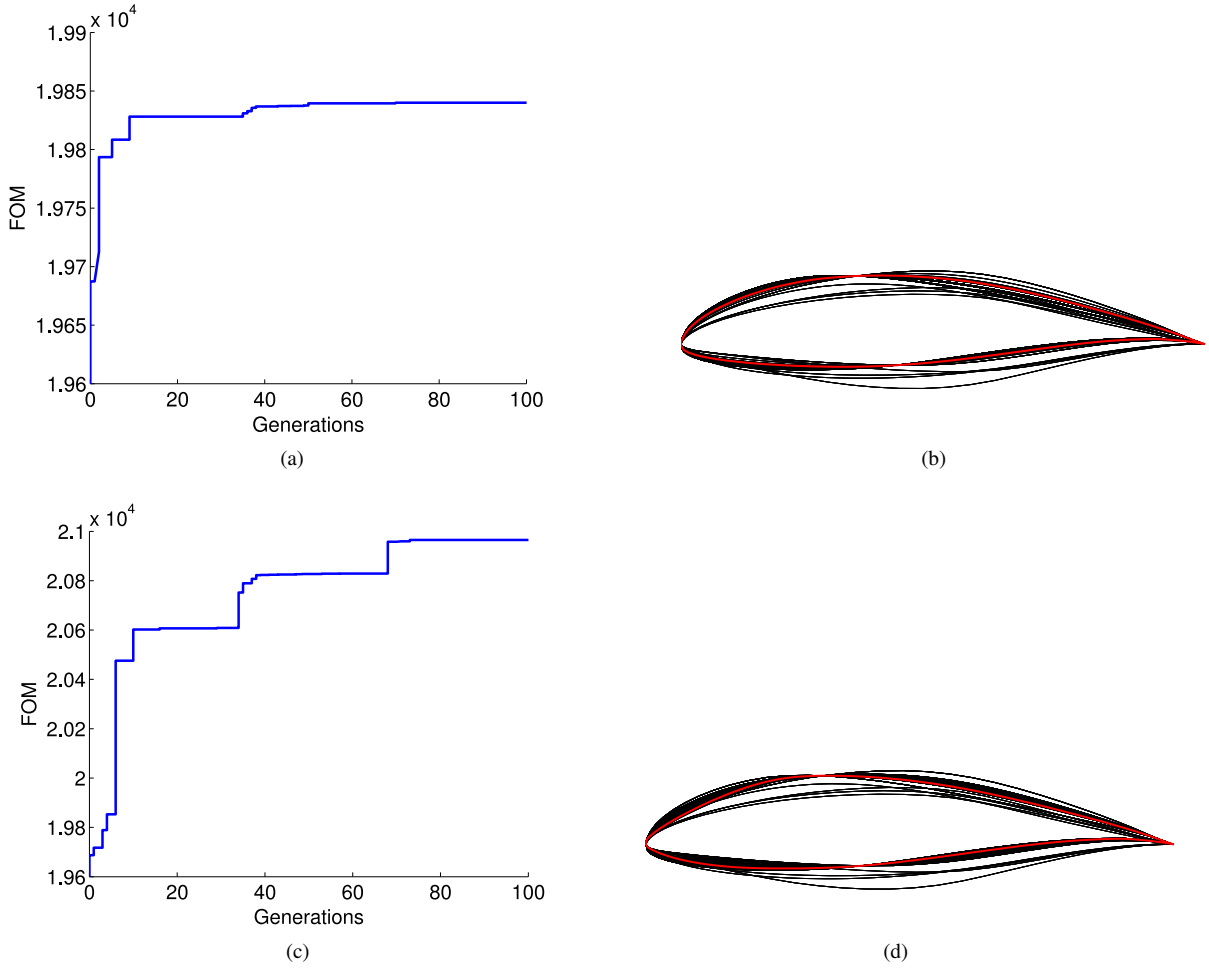

Figure 13. Global airfoil optimization: (a) and (c) best FOM, (b) and (d) best airfoils at each selection, using no LE perturbations, and using LE perturbations respectively; red airfoils: best individuals; $t/c = 18\%$, sand grain diameter $d = 200$ μm, $C_l = 1$.

for strong and localized LE suction peaks. An unfavorable boundary layer growth is expected in that region with possible early separation and a significant drop in aerodynamic performance (increase in C_d and decrease in C_l).

An important piece of information derived from Figs. 13 and 14 relates to the airfoil camber. Since the current approach is based on airfoil blending, the optimal shapes are free to vary in camber through the GA optimization method. Both optimal airfoils have a pronounced camber with respect to the optimal airfoils of Section IV. A. 2. As the GA optimization progresses, the increase in camber is due to an upward shift of both the lower and upper surfaces of the airfoils [Figs. 13(b) and 13(d)]. It can be concluded that cambered airfoils allow for weaker suction peaks on the upper side for a given lift coefficient C_l when compared with non-cambered airfoils operating at the same C_l. Such feature allows for the particles to impact the upper surface at a reduced velocity, hence promoting smaller values of E. On the lower side, a flat surface allows for the particle to slow down more, hence reducing the erosive effect.

The optimization of wind turbine airfoils through geometry perturbations shows its flaws due to the limited design space and to the aerodynamic performance tied to that. In other words, since the design space is small, also is the capability of investigating *good* airfoil geometries. Finally, it has to be noted that by selecting different pools of airfoils, the algorithm would have different outcomes of the optimal airfoil.

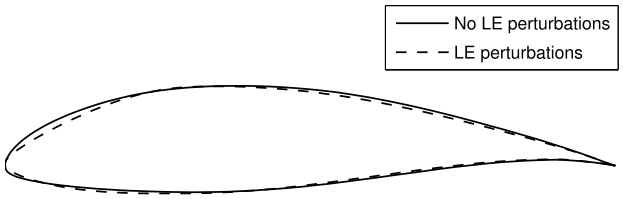

Figure 14. Comparison of global airfoil optimization.

Table 3. Figures of Merit of the Global Optimization and Comparison with State-of-the-Art

Airfoil	FOM	$\%\Delta_{FOM}$
DU 96-W-180	14608	-
no LE perturbations	19840	35.8
LE perturbations	20965	43.5

B. Genetic Optimization Through Airfoil Inverse Design

However complex, an optimization that makes use of pre-existing geometries is intrinsically limited. In the current section, the optimization is performed using airfoil inverse design so that this issue is overcome. The algorithm with such a capability is PROFOIL,[51,52] which is included in the GA wrapper and called at each airfoil generation in order to obtain the geometry of the new individual. PROFOIL makes use of a conformal mapping technique to design airfoils. In particular, it allows the user to prescribe the velocity distribution over an airfoil by means of the α^*-ϕ distribution. A detailed explanation of the inverse design method is beyond the scope of this paper, and the authors suggest referring to the published literature for further details.[51,52]

In order to assess the aerodynamic properties of the airfoil, the aerodynamic polars are included in the current approach. By doing so, the optimization allows to maximize FOM without penalizing $(C_l/C_d)_{max}$, effectively becoming a two-objective optimization. The classic approach for these type of problems is by using the Pareto front criteria.[50] The aerodynamic polars are evaluated by also including XFOIL in the GA wrapper.[34]

Since a few steps in the GA scheme are now different from the direct airfoil design, the new steps of the code can be summarized as follows:

1. A population of randomly generated airfoils is initalized. In particular, PROFOIL is initialized with random values of α^*, while ϕ are kept constant,
2. α^* of two airfoils (parents) are combined in a random fashion to obtain a new generation (crossover),
3. Random perturbations on the airfoil properties may be included randomly to increase specie diversity, in the form of $\Delta\alpha^*$ (mutation),
4. The constraints are imposed: typically C_l or α, and $(t/c)_{max}$,
5. The aerodynamic polar of the airfoil is computed through XFOIL. The value of $(C_l/C_d)_{max}$ is computed (evaluation),
6. The particle code BugFoil is executed and FOM is also computed (evaluation),
7. FOM and $(C_l/C_d)_{max}$ are written into a logfile,
8. The Pareto front is computed, and the parents for the following generation are selected amongst the individuals lying on the Pareto front,
9. The algorithm proceeds back to step 2) until the number of maximum generations is reached or convergence is obtained.

Table 4. Values of the α^*-ϕ Distribution Used for the Airfoil Inverse Design

Pair	α^* (deg)	ϕ (deg)
1	10.0	15.5
2	unconstrained	19.5
3	unconstrained	25.5
4	unconstrained	32.2
5	unconstrained	45.5
6	4.0	60.0

It can be immediately seen that the computational time of this approach is increased due to the aerodynamic computations of XFOIL. In fact, the evaluation of C_l and C_d with reasonable increments in angle of attack ($\Delta\alpha = 0.3$ deg) increases considerably the runtime of the code. Also, it should be noted that on modern machines PROFOIL can be executed in less than 1/10 of a second, thus not hurting the overall computational time. In general, an average of 10 seconds were required to evaluate each airfoil.

1. Results

An extensive test of PROFOIL was performed to decide the parameters to be used for the GA scheme. By doing so, the goal was to reduce the computational time of the optimization and avoid expanding the design space to unfeasible airfoil geometries or to airfoils with limited aerodynamic performance. Also, because the most prominent effects of particle erosion are seen toward the blade tip, the airfoil t/c and moment coefficient C_m were set equal to those of an outboard-region airfoil – the DU 96-W-180 (t/c =18%, C_m = -0.063).

Particular care was taken to select the number of pairs in the α^*-ϕ distribution. It was observed that increasing the number of such pairs increased the computational time noticeably. Moreover, a large number of α^*-ϕ would only allow for modest improvements in $(C_l/C_d)_{max}$. For these reasons, the number of pairs was set to six, and α^* were set unconstrained on the interval (-1 – 13) deg. Table 4 shows the parameters used for the inverse design GA. Since the approach used in this phase encompasses the widest of the design spaces investigated thus far, the number of individuals for each generation was raised significantly, and the maximum number of iterations was raised to 120. At the end of each optimization an average of 5,000 individuals were sampled, yielding a total computational time that varied between 12 and 20 hr.

The first inverse design optimization is performed at the same conditions as for the direct airfoil design ($d = 200$ μm, $V_\infty = 69.4$ m/s, $c = 1.7$ m, and $C_l = 1$), equivalent to $Re = 6.88\times10^6$ for a blade section located at $r/R = 0.75$ along the bladespan. The results of the optimization are reported in Fig. 15. The first information that appears is related to the high values of $(C_l/C_d)_{max}$ as shown in Fig. 15(a). A steady $(C_l/C_d)_{max} = 324.62$ is reached as early as 31 generations, while the FOM plateaus earlier [Fig. 15(b)]. However, the most relevant information comes from analyzing the history of the best geometries shown in Fig. 15(c). Similar to the direct airfoil design optimization, a progressive increase in airfoil camber is also observed here. In fact, the lower surface reaches an almost flat configuration, followed by a slightly cambered shape. The upper surface moves upward accordingly, and the upper portion of the leading edge appears bulbous. These observations are in good agreement with the earlier phases of the study. The authors also found in the recent published literature a similar optimization study by He et al.[57] The shape optimization of a wind turbine airfoil to maximize $(C_l/C_d)_{max}$ was investigated, and similar trends in the displacement of upper and lower surfaces were observed. The reason behind such high values of $(C_l/C_d)_{max}$ observed in the current study has to be found in the recovery region behind the location of maximum thickness on the airfoil upper surface. This portion of the airfoil acts as a Stratford recovery region which represents a technique used for high lift airfoil design.[58]

As most of blade erosion occurs toward the blade tip, a second optimization was performed for a blade section located in the tip region at $r/R = 0.95$. At such location, the wind turbine blade has a small chord ($c = 1.0$ m), while the local velocity is increased to $V_\infty = 84.9$ m/s. The resulting Reynolds number is now $Re = 5.84\times10^6$, but the relevant information comes from the nondimensional mass AK of the sand particle. In fact, by keeping the diameter to $d = 200$ μm, AK is now greater than for a blade section located at $r/R = 0.75$ (see Eq. 13). In other words, a short blade section has less aerodynamic influence on a particle than a large blade section. Therefore, the optimization is expected to show a smaller influence of the blade shape with respect to erosion.

The optimization of the blade section located at $r/R = 0.95$ is shown in Fig. 16. It can be seen that both $(C_l/C_d)_{max}$

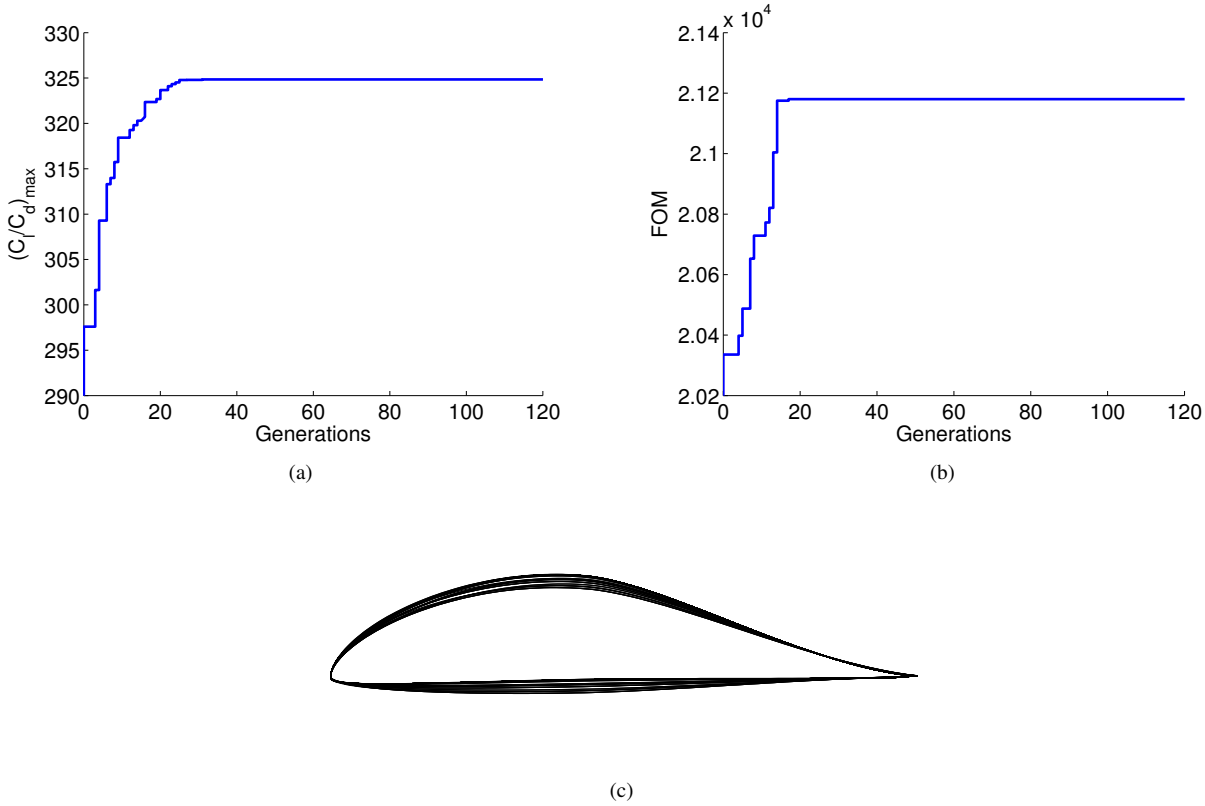

Figure 15. History of inverse airfoil optimization: (a) $(C_l/C_d)_{max}$, (b) best FOM, and (c) best airfoils at each selection; $r/R = 0.75$, $t/c = 18\%$, $C_m =$ -0.063, sand grain diameter $d = 200$ μm, $C_l = 1$.

[Fig. 16(a)] and FOM [Fig. 16(b)] reach a plateau later than for the $r/R = 0.75$ optimization [see Figs 15(a) and 15(b)]. Also, both $(C_l/C_d)_{max}$ and best FOM are smaller than for the airfoil located at $r/R = 0.75$. Finally, the geometry history shown in Fig. 16(c) shows smaller variations in the best airfoils as compared with the more inboard section [Fig. 15(c)]. This result can be seen as a smaller influence of the airfoil on the particle trajectory; therefore, the best $(C_l/C_d)_{max}$ plateaus at 311.03. It should be noted that due to the high particle impact velocity at $r/R = 0.95$, FOM is also lower, since it is a function of $1/E_{max}$.

A comparison of both $(C_l/C_d)_{max}$ and FOM with the DU 96-W-180 airfoil is presented in Table 5. The two airfoils designed with inverse design process outperform the DU 96-W-180 airfoil both in FOM and in $(C_l/C_d)_{max}$. However, such a margin becomes smaller as the considered blade section is moved outboard. Again, this is due to the reduced effect of the flowfield on the particle at such locations.

V. Conclusions

This paper presents the optimization of wind turbine airfoils subject to sand erosion. The effect of sand impingement on the blade surface is translated into two peaks of maximum erosion rate E located at a distance from the LE. Both erosion peaks are subject to shifts due to angle of attack, particle diameter, and inflow velocity. Moreover, it was seen that the aerodynamic performance of a damaged airfoil due to sand erosion depends on the location of the damage along the chord length.

The role of different airfoil shapes with respect to erosion rate was also investigated. It was found that a bulbous upper leading edge promotes the erosion rate peak to move downstream; on the other hand, a flat slanted LE lower surface allows for the particles to slow down more and hit the surface at near-normal angles. The erosion rate of plastic

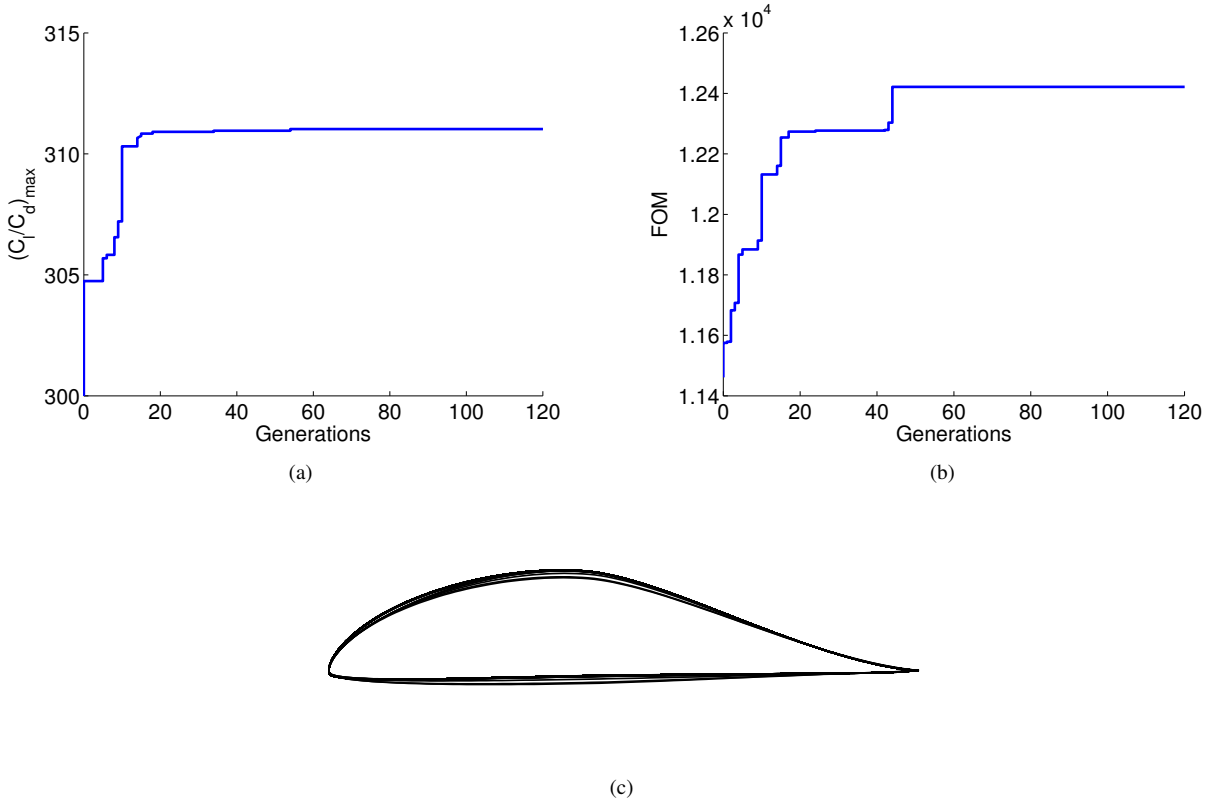

Figure 16. History of inverse airfoil optimization: (a) $(C_l/C_d)_{max}$, (b) best FOM, and (c) best airfoils at each selection; $r/R = 0.95$, $t/c = 18\%$, $C_m =$ -0.063, sand grain diameter $d = 200$ μm, $C_l = 1$.

Table 5. Comparison of FOM and $(C_l/C_d)_{max}$ with State-of-the-Art Airfoils.

Airfoil	r/R	FOM	$\%\Delta_{FOM}$	$(C_l/C_d)_{max}$	$\%\Delta_{(C_l/C_d)_{max}}$
DU 96-W-180	0.75	14608	-	174.18	-
DU 96-W-180	0.95	10815	-	172.14	-
Inverse Design	0.75	21180	44.9	324.62	86.4
Inverse Design	0.95	12422	14.9	311.03	80.7

materials shows a minimum for such impact angles; therefore, near-normal impact angles are favorable in the lower region. Based on these findings, a figure of merit FOM was formulated.

The optimization of the airfoil geometry was undertaken by multiple formulations of a genetic algorithm approach. In particular, a direct airfoil design approach was used to return initial insights on the optimal shapes required to maximize an erosion figure of merit FOM. In this approach, the aerodynamic performance of the airfoil was disregarded temporarily. The first direct design algorithm investigated optimal LE shapes only, while the second phase investigated optimal shapes by blending existing airfoil geometries. In the latter case, better FOM values were obtained compared with the LE optimization only results. Due to the intrinsically small design space of a direct design approach, a more powerful and robust inverse design method (PROFOIL) was implemented in the GA code. Such an approach allowed optimized airfoils to reach high values of $(C_l/C_d)_{max}$ while also obtaining high values in FOM. In particular, a $(C_l/C_d)_{max}$ of 324.62 was obtained for an airfoil located at $r/R = 0.75$. Finally, the optimization by means of inverse design outperformed the best FOM obtained in every previous optimization methods of the study.

The airfoil design optimization pursued in this paper can be used to select the airfoils based on the results of erosive damage. A better performing airfoil with respect to sand erosion will have better aerodynamic performance once the damage has been initiated on the blade surface when compared with a classic wind turbine airfoil. Such an airfoil not only it allows for the wind turbine blade to operate at higher values of $(C_l/C_d)_{max}$ in the turbine initial clean conditions, but also to mitigate the effects of the erosion as the blade ages.

VI. Acknowledgments

The author would like to thank Ali El-Ashri for his help and enthusiasm during the development of the GA code. Also gratitude goes to Kyle Tsai for his insights and help during the latest part of the code implementation.

References

[1]Dalili, N., Edrisy, A., and Carriveau, R., "A Review of Surface Engineering Issues Critical to Wind Turbine Performance," *Renewable and Sustainable Energy Reviews*, Vol. 13, 2007, pp. 428–438.

[2]Sagol, E., Reggio, M., and Ilinca, A., "Issues Concerning Roughness on Wind Turbine Blades," *Renewable and Sustainable Energy Reviews*, Vol. 23, 2013, pp. 514–525.

[3]Ahmed, M. R., "Blade Sections for Wind Turbine and Tidal Current Turbine Applications – Current Status and Future Challenges," *International Journal of Energy Research*, Vol. 36, 2012, pp. 829–844.

[4]Hayman, B., Wedel-Heinen, J., and Brondsted, P., "Materials Challenges in Present and Future Wind Energy," *MRS Bulletin*, Vol. 33, April 2008, pp. 343–353.

[5]Singh, S., Bhatti, T. S., and Kothari, D. P., "A Review of Wind-Resource-Assessment Technology," Centre for Energy Studies, Indian Institute of Technology. Hauz Khas, New Delhi 110016, 2012.

[6]Ciang, C. C., Lee, J. R., and Bang, H. J., "Structural Health Monitoring for a Wind Turbine System: a Review of Damage Detection Methods," *Measurement Science and Technology*, Vol. 19, No. 12, Oct. 2008, pp. 122001–122021.

[7]Huang, C. W., Yang, K., Liu, Q., Zhang, L., Bai, J. Y., and Xu, J. Z., "A Study on Performance Influences of Airfoil Aerodynamic Parameters and Evalutation Indicators for the Roughness Sensitivity on Wind Turbine Blade," *Science China - Technological Sciences*, Vol. 54, No. 11, 2011, pp. 2993–2998.

[8]Mayor, G. S., Moreira, A. B. B., and Munoz, H. C., "Influence of Roughness in Protective Strips of Leading Edge for Generating Wind Profiles," *22nd International Congress of Mechanical Engineering*, COBEM 2013, 2013.

[9]Soltani, M. R., Birjandi, A. H., and Seddighi-Moorani, M., "Effect of Surface Contamination on the Performance of a Section of a Wind Turbine Blade," *Scientia Iranica B*, Vol. 18, No. 3, 2011, pp. 349–357.

[10]Ren, N. and Ou, J., "Dust Effect on the Performance of Wind Turbine Airfoils," *Journal of Electromagnetic Analysis and Applications*, Vol. 1, No. 2, 2009, pp. 102–107.

[11]Sareen, A., Sapre, C. A., and Selig, M. S., "Effects of Leading-Edge Protection Tape on Wind Turbine Blade Performance," *Wind Engineering*, Vol. 36, No. 5, 2012, pp. 525–534.

[12]van Rooij, R. P. J. O. M. and W.A.Timmer, "Roughness Sensitivity Considerations for Thick Rotor Blade Airfoils," *Proceedings of the 41st Aerospace Sciences Meeting and Exhibit*, AIAA Paper 2003-350, 2003.

[13]Arrighetti, C., Pratti, G. D., and Ruscitti, R., "Performance Decay Analysis of New Rotor Blade Profiles for Wind Turbines Operating in Offshore Environments," *Wind Engineering*, Vol. 27, No. 5, 2003, pp. 371–380.

[14]Ragheb, A. and Selig, M. S., "Multi-Element Airfoil Configurations for Wind Turbines," *Proceedings of the 29th AIAA Conference*, AIAA Paper 2011-3971, 2011.

[15]Schneiderhan, T., Schulz-Stellenfleth, J., Lehner, S., and Hortsmann, J., "Sar Wind Fields for Offshore Wind Farming," DLR, Oberpfaffenhofen, 82230 Wessling, Germany, 2002.

[16]DNV, "Design and Manufacture of Wind Turbine Blades, Offshore and Onshore Wind Turbines - October 2010," Standard DNV-DS-J102, Det Norske Veritas, Oct 2010.

[17]Khakpour, Y., Bardakji, S., and Nair, S., "Aerodynamic Performance of Wind Turbine Blades in Dusty Environments," *International Mechanical Engineering Congress and Exposition, Seattle, Washington*, IMECE2007-43291, 2007.

[18]Tilly, G., "Erosion Caused by Airborne Particles," *Wear*, Vol. 14, No. 1, 1969, pp. 63–79.

[19]Davis, J. R., editor, *Surface Engineering for Corrosion and Wear Resistance*, chap. 3, ASM International - The Materials Information Society, 10M Communications, Materials Park, OH 44073-0002, 2001, pp. 43–86.

[20]Wood, R. J. K., "The Sand Erosion Performance of Coatings," *Materials and Design*, Vol. 20, No. 4, 1999, pp. 179–191.

[21]Tabakoff, W. and Balan, C., "A Study of the Surface Deterioration due to Erosion," *Proceedings of the 28th ASME Interational Gas Turbine Conference and Exhibit, Phoenix, Arizona*, Vol. 105, 1983, pp. 834–838.

[22]Fiore, G. and Selig, M. S., "A Simulation of Operational Damage for Wind Turbines," *Proceedings of the 32nd AIAA Applied Aerodynamics Conference*, AIAA Paper 2014–2848, 2014.

[23]Keegan, K. H., Nash, D. H., and Stack, M. M., "Modelling Rain Drop Impact of Offshore Wind Turbine Blades," *Proceedings of the TURBO EXPO*, 2012.

[24]Keegan, K. H., Nash, D., , and Stack, M., "Numerical Modelling of Hailstone Impact on the Leading Edge of a Wind Turbine Blade," Workshop paper, University of Strathclyde, Department of Mechanical and Aerospace Engineering, Glasgow, UK, 2013.

[25]Fiore, G., Fujiwara, G. E. C., and Selig, M. S., "A Damage Assessment for Wind Turbine Blades from Heavy Atmospheric Particles," *Proceedings of the AIAA Conference, Kissimmee, FL*, AIAA Paper 2015–1495, 2015.

[26]Zahavi, J. and Nadiv, S., "Indirect Damage in Composite Materials Due to Raidrop Impact," *Wear*, Vol. 72, 1981, pp. 305–313.

[27]Kensche, C. W., "Fatigue of Composites for Wind Turbines," *International Journal of Fatigue*, Vol. 28, 2006, pp. 1363–1374.

[28]McGechaen, R. and Stack, M. M., "A Study of Raindrop Erosion of Steel and Polymer Based Composites: Application to Wind Turbines," Department of Mechanical Engineering, University of Strathclyde, James Weir Building, 75 Montrose St., Glasgow, G1 1XJ, Oct 2013.

[29]Springer, G. S., *Erosion by Liquid Impact*, Scripta Technica, Inc., Washington, D.C., 1976.

[30]Wood, K., "Blade Repair: Closing the Maintenance Gap," Composites World, Apr 2011, URL `http://www.compositesworld.com`.

[31]Challener, C., "Coatings Critical for Wind Energy Efficiency," JCT CoatingsTech, Jan 2010.

[32]Keegan, M. H., Nash, D. H., and Stack, M. M., "On Erosion Issues Associated with the Leading Edge of Wind Turbine Blades," *Journal of Physics D: Applied Physics*, Vol. 46, 2013, pp. 1–20.

[33]Bragg, M. B. and Maresh, J. L., "A Numerical Method To Predict The Effect of Insect Contamination on Airfoil Drag," Aeronautical and Astronautical Engineering Report AARL 86-01, The Ohio State University Research Foundation, OH 43212, Mar 1986.

[34]Drela, M., "XFOIL: An Analysis and Design System for Low Reynolds Number Airfoils," *Low Reynolds Number Aerodynamics*, edited by T. J. Mueller, Vol. 54 of *Lecture Notes in Engineering*, Springer-Verlag, New York, June 1989, pp. 1–12.

[35]Roskam, J., *Airplane Flight Dynamics and Automatic Flight Controls*, DARcorp, Lawrence, KS 66044, 1995.

[36]Bragg, M. B., "Rime Ice Accretion and Its Effect on Airfoil Performance," NASA Lewis Research Center, NASA CR-165599, Mar 1982.

[37]Langmuir, I. and Blodgett, K., "Mathematical Investigation of Water Droplet Trajectories," Tech. Rept. 5418, U.S. Army Air Force, 1946.

[38]Hamed, A. A., Tabakoff, W., Rivir, R. B., Das, K., and Arora, P., "Turbine Blade Surface Deterioration by Erosion," *Journal of Turbomachinery*, Vol. 127, No. 3, 2005, pp. 445–452.

[39]J. Zahavi and G. F. Schmitt Jr., "Solid Particle Erosion of Polymeric Coatings," *Wear*, Vol. 71, No. 2, 1981, pp. 191–210.

[40]Arjula, S., Harsha, A. P., and Ghosh, M. K., "Solid-Particle Erosion Behavior of High-Performance Thermoplastic Polymers," *Journal of Material Science*, Vol. 43, No. 6, 2008, pp. 1757–1768.

[41]Harsha, A. P. and Thakre, A. A., "Investigation on Solid Particle Erosion Behaviour of Polyetherimide and Its Composites," *Wear*, Vol. 262, No. 7–8, 2007, pp. 807–818.

[42]Barkoula, N.-M. and Karger-Kocsis, J., "Review – Processes and Influencing Parameters of the Solid Particle Erosion of Polymers and Their Composites," *Journal of Materials Science*, Vol. 37, 2002, pp. 3807–3820.

[43]Maozhong, Y., Baiyun, H., and Jiawen, H., "Erosion Wear Behaviour and Model of Abradable Seal Coating," *Wear*, Vol. 252, No. 1–2, 2002, pp. 9–15.

[44]Sareen, A., Sapre, C. A., and Selig, M. S., "Effects of Leading Edge Erosion on Wind Turbine Blade Performance," *Wind Energy*, Vol. 17, 2014, pp. 1531–1542.

[45]Timmer, W. A. and Rooij, R. P. J. O. M. V., "Summary of the Delft University Wind Turbine Dedicated Airfoils," *Proceedings of the 41st Aerospace Sciences Meeting and Exhibit*, AIAA Paper 2003-352, 2003.

[46]Timmer, W. A. and van Rooij, R. P. J. O. M., "Summary of the Delft University Wind Turbine Dedicated Airfoils," *Journal of Solar Energy Engineering*, Vol. 125, No. 4, 2003, pp. 571–596.

[47]Tangler, J. L., "The Evolution of Rotor and Blade Design," *Presented at the American Wind Energy Association, Wind Power 2000*, NREL CP-500-28410, 2000.

[48]Tangler, J. L. and Somers, D. M., "NREL Airfoil Families for HAWTs," Nrel/tp-442-7109, NREL, 1617 Cole Boulevard, Golden, Colorado, 80401-3393, 1995.

[49]Buhl, M., 'Wind Turbine Airfoil Families," NREL, Jul 2012, URL `https://wind.nrel.gov/airfoils/AirfoilFamilies.html`.

[50]Schwefel, H.-P., editor, *Evolution and Optimal Seeking*, chap. 5, John Wiley and Sons, Inc., 605 Third Avenue, New York, NY, 1994, pp. 105–164.

[51]Selig, M. S. and Maughmer, M. D., "A Multi-Point Inverse Airfoil Design Method Based on Conformal Mapping," *AIAA Journal*, Vol. 30, No. 5, 1992, pp. 1162–1170.

[52]Selig, M. S. and Maughmer, M. D., "Generalized Multipoint Inverse Airfoil Design," *AIAA Journal*, Vol. 30, No. 11, 1992, pp. 2618–2625.

[53]Gardner, B. A. and Selig, M. S., "Airfoil Design Using a Genetic Algorithm and an Inverse Method," *Proceedings of the 41st Aerospace Sciences Meeting and Exhbit, Reno, NV*, AIAA Paper 2003–0043, 2003.

[54]Vicini, A. and Quagliarella, D., "Inverse and Direct Airfoil Design Using a Multiobjective Genetic Algorithm," *AIAA Journal*, Vol. 35, No. 9, 1997, pp. 1499–1505.

[55]Bizzarrini, N., Grasso, F., and Coiro, D. P., "Genetic Algorithms in Wind Turbine Airfoil Design," *Proceedings of the 2011 European Wind Energy Association Conference*, EWEA, 2011.

[56]Yumusak, M. and Eyi, S., "Aerothermodynamic Shape Optimization of Hypersonic Blunt Bodies," *21st AIAA Computational Fluid Dynamics Conference, San Diego, CA*, AIAA Paper 2013-265, 2013.

[57]He, Y. and Agarwal, R. K., "Shape Optimization of NREL S809 Airfoil for Wind Turbine Blades Using a Multiobjective Genetic Algorithm," *International Journal of Aerospace Engineering*, Vol. 14, No. 1, 2014, pp. 1–14.

[58]Liebeck, R. H. and Ormsbee, A. I., "Optimization of Airfoils for Maximum Lift," *Journal of Aircraft*, Vol. 7, No. 5, 1970, pp. 409–415.